Silicon (2018) 10:1991–1997
https://doi.org/10.1007/s12633-017-9711-1

ORIGINAL PAPER

# Fractal Growth of Ferrite Nanoparticles Prepared by Citrate-Gel Auto-Combustion Method

**M. H. Abdellatif[1] · A. A. Azab[1]**

Received: 11 September 2017 / Accepted: 5 December 2017 / Published online: 17 April 2018


**Abstract**
We report a tree fractal growth of ferrite nanoparticles prepared by Citrate-Gel Auto-Combustion method. We compared the growth pattern of $CuFe_2O_4$, $Cr_2FeO_4$, $CdFe_2O_4$, $MgFe_2O_4$, and $Li_2Fe_3O_5$. The ferrite 3D growth was found to follow Family-Vicsek fractal growth in which the next added particle is looking for the best 3D orientation to minimize its surface free energy. The nanoparticles position in the sites of the growing tree forms a pattern that depends on the temperature, particle size, the orientation of the first seed particle and the particle to particle interaction forces. The results showed that the fractal arrangement is more preferred in the thermal growth of nanoparticles.

**Keywords** Fractal growth · Nanoparticles · Ferrite synthesis

## 1 Introduction

Particle dynamics expressed in Self-assembly [1, 2], aggregation phenomena [3] are accompanied by a characteristic geometrical pattern that can be described as a fractal [4–6]. These patterns are sensitive to the crystal structure of the nanoparticles, preparation method, and the interaction forces between the nanoparticles that form their aggregation pattern [3]. The concept of fractals has been introduced for the first time by Mandelbrot [7], since that time it has been used to interpret diverse of phenomena on the basis of geometry even though the interaction may not be geometrical in nature [8, 9]. A crucial parameter known as the fractal dimension is a non-integer number $D_f$, that is used to describe the structural and the dynamical properties. The fractal dimension represents the scaling of the density as a function of volume. Recent experimental reports showed that fractal patterns can be formed by controlling the dynamics of particle aggregation from a drop casted colloidal solution [1, 8–10]. To understand the dynamics of particles aggregation several trials have been made to investigate the fractal pattern formation and its dependence on the growth temperature, substrate roughness, deposition rate, impurities and inter-particle interaction energies [9–12]. However, the kinetics of the nanoparticles aggregation still not well understood. The heat generated by the exothermic reaction of the auto-combustion method is one reason for the induced fractal growth in the ferrite tree [11]. The schematic diagram of that reaction is depicted in ref [13]. The high formation temperature in the sol-gel method can reach 600 to 1350 $^{o}$C, which allows particle migration during the aggregation process [14–16]. The auto-combustion technique has been applied successfully to fabricate different types of ferrites, such as Ni, Zn, Co, Cu, Li, Mg, Cd, Mn and their combinations as well [13, 17–25]. However the geometry of the growing ferrite tree depends on the kinetics of the inter-particles interaction forces that define the favored sites for the layer by layer growth. The growth is then can be explained on the basis of the diffusion limited aggregation model proposed by Witten and Sander [26].

In this work, we report a fractal growth of ferrite nanoparticles tree prepared by sol-gel auto-combustion technique. We compared the fractal dimension of five different types of ferrite trees, and correlated the obtained results to the dopant cation size and the crystal lattice size. We discussed the relation of the formed pattern and the interparticle interaction forces that affect the layer by layer growth according to the diffusion limited growth model.

✉ M. H. Abdellatif
cds.moh@gmail.com

[1] Solid State Physics Department, Physics Division, National Research Center, Dokki, Giza, P.O.12622, Egypt

We also showed that parameters such as the fractal dimension, crystal size and the residual strain of the ferrite crystal structure are correlated.

## 2 Experimental

$CuFe_2O_4$, $Cr_2FeO_4$, $CdFe_2O_4$,$MgFe_2O_4$ and $Li_2Fe_3O_5$ ferrite nanoparticles were synthesized by the citrate-gel auto-combustion technique using the source materials ferric nitrate ($Fe(No_3)_3.9H_2O$), copper nitrate ($Cu(NO_3)_2.3H_2O$), lithium nitrate (Li $NO_3.3H_2O$), cadmium nitrate ($(Cd(NO_3)_2.4H_2O$), chromium nitrate ($Cr(NO_3)_3.9H_2O$), magnesium nitrate ($Mg(NO_3)_2.6H_2O$). The metal nitrates were dissolved in 100 ml of distilled water and stirred for 15 min, and then citric acid was added in a ratio of 1:1 to metal nitrates solution. Ammonia droplets of 33% concentration were added to adjust the pH of the mixture to 7. The solution was continuously stirred at 130 °C and then was transferred into xerogel. The dried gel burns in self-propagating combustion to form the ferrite nanostructure. Ferrite preparation using Sol-Gel method induces an anionic redox reaction of xerogel using exothermic self-sustaining reaction. The reaction causes a rapid release of gasses with a great mass loss leading to ferrite nanopowder formation. The nanopowder grows in a tree like a shape that has clear fractal geometry. The structural properties of the ferrite powder were investigated by X-ray diffraction (XRD; Proker D8) with $CuK_\alpha$ radiation of wavelength 1.5481 Åat room temperature. The fractal dimensions were calculated using the box counting method [27, 28]. High-quality images of the ferrite tree are taken and converted to monochromatic contours in order to calculate the fractal dimension using box counting method [29].

## 3 Results and Discussion

Figure 1 shows a schematic diagram of the spinel ferrite crystal structure of general formula $AB_2O_4$. Spinel ferrite is known to have two interstitial sites, octahedral and tetrahedral sites in which cations occupy the sites according to their valence and ionic radii. The structure can be described as a cubic closed packed arrangement of oxygen atoms in which 32 ions form a unit cell. The structure contains 64 tetrahedral sites and 32 octahedral sites. Only 8 tetrahedral sites and 16 octahedral sites are occupied by divalent or trivalent ions. The arrangement takes place to keep the unit cell electrically neutral. Structurally, there are three types of ferrites [15]. The general formula of spinel ferrite $AB_2O_4$ can be represented: $(A_{1-\delta}B_\delta)$ $[B_{2-\delta}A_\delta]O_4$, where A, B represent a divalent and trivalent cations, $\delta$ is the inverse degree, if $\delta = 0$ then ferrite is described

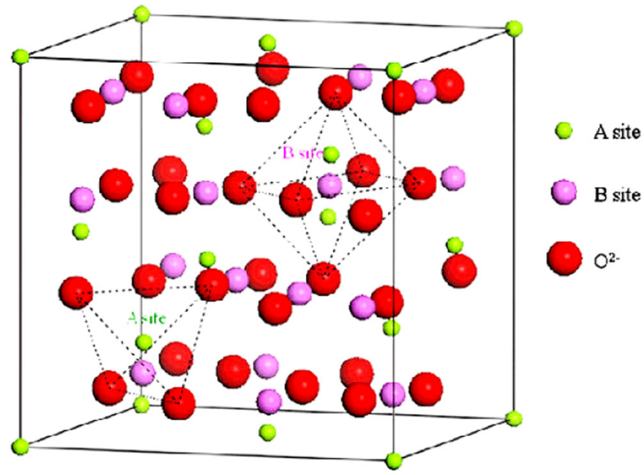


**Fig. 1** Structure of spinel ferrite, showing interstitial tetrahedral (green balls), and octahedral sites (cyan balls), red balls represent the oxygen cations

as normal ferrite, $\delta = 1$ represent inverse ferrite, and $0<\delta<1$ represent mixed spinel ferrite [30–33]. In the formation stage reagents are very important, the reagents can effectively chelate the metal ions with different size and prevent selective precipitation of the metal ions and stabilize the homogeneity among precipitation, also prevent the release of toxic gasses [11]. Reagents differ in the amount of the released gasses, toxicity, and the reduction power in the reaction. Accordingly, the reaction conditions play an important role in the final product purity and homogeneity and the charge transfer in the ferrite structure. All these parameters affect the final growth geometry that can be represented by the fractal structure. The effect of the reagent on the spinel structure has been widely studied [11, 34–38]. It was reported that the heat generated by using glycine, urea and citric acid was -3.24 kcal/g, -2.981 kcal/g and -2.76 kcal/g, respectively [39]. Another factor is the oxygen balance which is an important factor of balancing the reaction to produce single phase ferrite. In principle, the number of valances in the salt should be balanced with the total valance in the reagent. If the reagents have oxygen deficiency then the heat released and gasses will be decreased, and the reaction takes a long time to take place. Moreover lower crystallinity and secondary phases can be also formed [15].

Figure 2 shows the X-ray diffraction patterns of $CuFe_2O_4$, $Cr_2FeO_4$, $CdFe_2O_4$, $MgFe_2O_4$ and $LiFe_2O_4$ ferrites prepared by using citric acid as a reagent. The results show that the prepared ferrites have one crystalline phase. The position of the diffraction peaks indicates the formation of the cubic spinel structure [40]. The data of $CuFe_2O_4$, $Cr_2FeO_4$, $CdFe_2O_4$, and $MgFe_2O_4$ were indexed according to JCPDS card No. 77-0010 in which the ferrites showed a preferred orientation along (311) direction. $CuFe_2O_4$

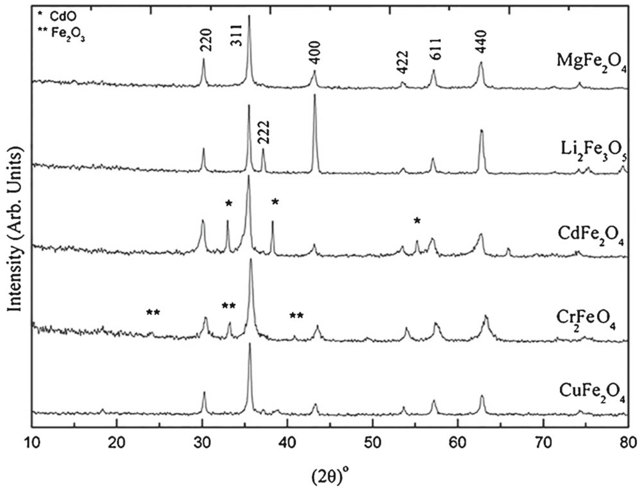


**Fig. 2** X-ray diffraction of different ferrites of Mg, Li, Cd, Cr and Cu ferrites

and $MgFe_2O_4$ are formed with a single phase, whereas the $CdFe_2O_4$ shows the existence of secondary phases, additional three peaks located at 32.91, 38.31 and 55.15° are found. These peaks arise from the presence of CdO which is indexed according to the standard card No. 75-0592. $Cr_2FeO_4$ sample contains also a secondary phase due to the presence of diffraction peaks at 24.15, 33.45 and 40.83°. These peaks are attributed to the presence of $Fe_2O_3$ as indexed according to the standard card No.89-8104. Besides, the diffraction peaks of $LiFe_2O_4$ showed a preferred orientation along (400) direction. The data were indexed to the cubic structure according to the standard card No. 41-0971 without secondary phases. The lattice parameter $a$, of the ferrites is determined from the well-known equation for the cubic system:

$$a = d\left(h^2 + k^2 + l^2\right)^{1/2} \tag{1}$$

Where $d$ is the interplanar spacing and $h$, $k$, $l$ is the Miller indices.

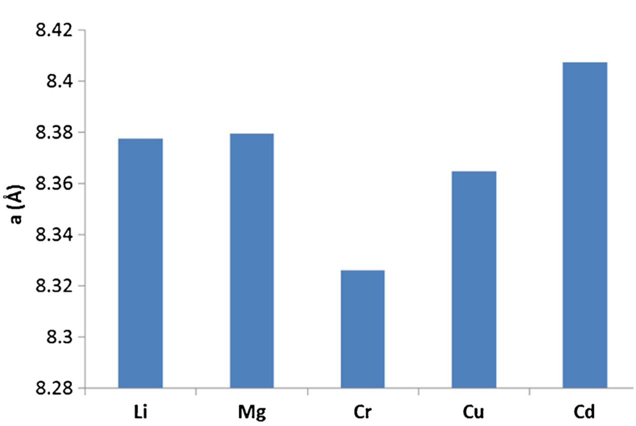


**Fig. 3** Lattice parameter of different ferrites

Figure 3 shows the calculated lattice parameter for the studied ferrites. It is noted that the smallest lattice parameter is assigned to $Cr_2FeO_{4x}$ in which ionic radii of $Cr^{3+}$ has the smallest value 0.615 Å [35], whereas the largest ionic radii for $Cd^{+2}$ (0.95 Å) [35] corresponds to the largest lattice parameter of $CdFe_2O_4$. Generally, the data of all ferrites reveal broadening in the diffraction peaks, the difference in doping affects also the optical, magnetic and electric properties [41–44]. Figure 4a-e shows the fractal pattern of the grown ferrites, in which different aggregation pattern depending on the type of doping cation is generated. To estimate the crystallite size and microstrain, we applied Williamson–Hall model:

$$\beta = \frac{K\lambda}{D\cos\theta} + 4\varepsilon\tan\delta \tag{2}$$

**Fig. 4** **a**-**e**: Image of as prepared ferrites showing the fractal patterns: **a** Cd-ferrite, **b** Cr-ferrite **c** Cu-ferrite, **d** Li-ferrite and **e** Mg-ferrite

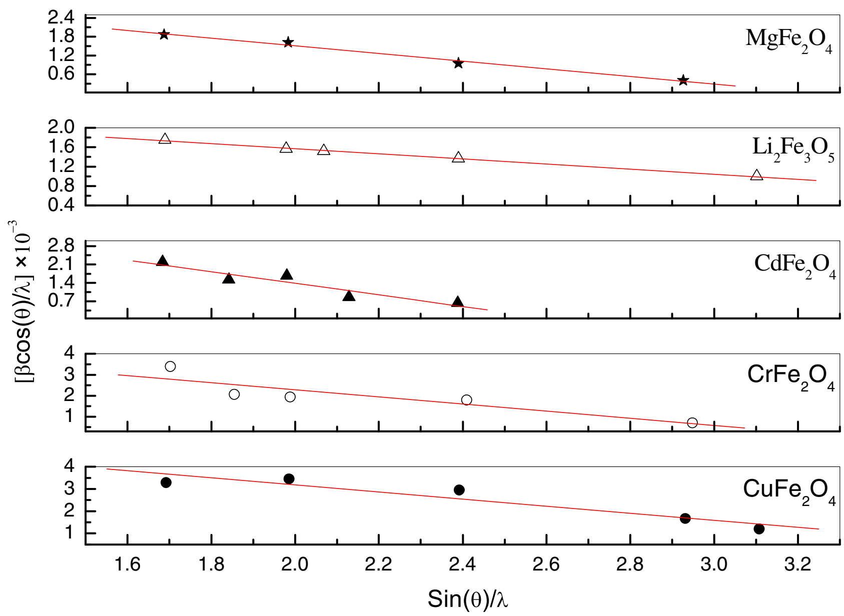


**Fig. 5** Williamson–Hall plots of different ferrites

Where β is the full-width half maximum of the diffraction peaks at 2θ, K is a dimensionless constant taken as 0.9, and λ is the wavelength of the X-ray used, D is the crystalline size and $\varepsilon$ is the microstrain. Figure 5 shows the relation between (βcosθ/λ) and (sinθ/λ) for the prepared ferrites. Accordingly, the crystalline size and microstrain is determined from the intercept and slope, respectively.

To understand the factors affecting the growth of the fractal pattern of different ferrites, consider a 3D nucleation growth of particles that evolve in time, in a layer by layer growth mode. In each layer, particles are added according to the conditions favored for lowering the surface free energy and the residual strain. Initially, all the sites are empty and the next layer evolution starts after occupying all the sites of the first layer. The next particle orientation and position are placed according to the interaction energy of the particle with its neighbors. This interaction energy $E_i$ is responsible for developing the final fractal pattern. The images in Fig. 5a-e show that the Williamson–Hall plot of the differently mixed ferrites. It can be concluded that the sum of all the interaction energies of the 3D grown pattern defines the ordination and porosity of the generated strcture.

The calculated crystalline size assigned to the fractal dimension for the investigated types of ferrites is shown in Fig. 6a. in which the oxidation state is the ruling factor in the graph [45]. Figure 6b depicts the increase of the residual strain as the ionic radii of cations increases providing that the corresponding fractal dimension also increases and saturate at around 2.88. The higher the fractal dimension, the higher the closed package and less porosity of the product. It is possible theoretically to engineer the porosity of the ferrite for sensing application by tuning the kinetics of thermal growth and controlling the it's fractal dimension, which is taken here as a measure for sample porosity.

Accordingly, the fractal dimension is found to increase with increasing the ionic radii of the cations. On the contrary, the crystalline size is found to decrease with increasing the ionic radii of cations, resulting in larger fractal dimension. The lowest fractal dimension as shown in Fig. 6 is Li ferrite with higher porosity and crystalline size of 35 nm while Cu ferrite has a fractal dimension of 2.5 and crystalline size of 15 nm. The data can be understood on the basis of the particle interaction energy. The particle interaction energy is known to be temperature dependent, it defines the probability of a particle to stay in certain position. The interaction energy eventually determines the fractal dimension of the ferrite's formed pattern. The probability, $P = \exp(-\beta\Delta E)$, where $\Delta E$ is the difference in energy between the lowest ground energy of the particle and the actual state at the occupied position. Where the condition of $\Delta E > 0$ is always satisfied, and the energy is measured in the values of $J/k_B$, where $k_B$ is the Boltzmann constant, and J is the measure for orientation of the particle at site i with respect to its neighbor at site j. If particles are oriented in the same direction, then energy is zero, if not then energy is J. where $E_i = F(J, i_j)$. In that sense, the growth function W of a length L and time evolution t can be defined as $W(L.t)\ \alpha\ t^{\beta}$, where β defines the growth exponent of the 3D structure. At saturation, when all sites are occupied the function turns to be $W \propto L^{\alpha}$, where $\alpha$ is the roughness exponent. This exponent is expressed as $z = \frac{\alpha}{\beta}$, where z is the dynamical exponent related to the growth over time $t$, $t = L^{Z}$ according to the Family-Vicsek scaling relation [3, 36, 46]. Hence, the relaxation of the particles, as they are evolving in a 3D structure, is following the pattern

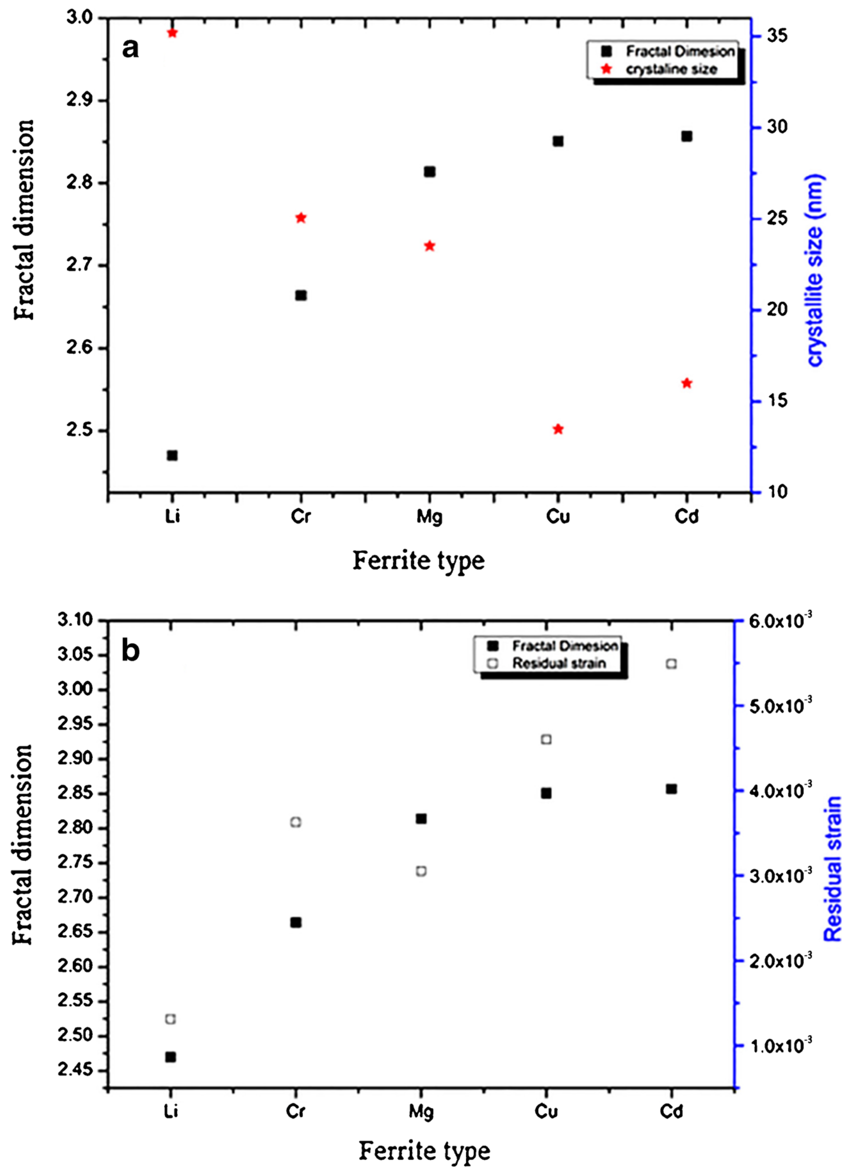


**Fig. 6** **a** Fractal dimension versus crystalline size for different ferrites. **b** Fractal dimension versus residual strain for different ferrites

that provides the minimum free energy. The lowest energy state provides less residual strain in the 3D structure, which corresponds to Li ferrite or bigger crystalline size. Hence, it can be concluded that the low value of fractal dimension for ferrites correspond to the low value of the residual strain, as it appears from the results of Williamson–Hall plot versus fractal dimension in Fig. 5.

## 4 Conclusion

We reported fractal pattern generation by the thermally induced growth of ferrite nanoparticles. Five types of ferrites namely $CuFe_2O_4$, $Cr_2FeO_4$, $CdFe_2O_4$, $MgFe_2O_4$, and $Li_2Fe_3O_5$, were prepared by thermally induced citrate-gel auto-combustion technique. The fractal growth could be explained in terms of diffusion limited aggregation for the irreversible growth of nanoparticles. The crystal size, microstrain and fractal dimension of the prepared ferrites showed that there is a correlation between the growth phenomena and the fractal dimension. The results showed an increase in the microstrain with increasing the fractal dimension, where the lowest fractal dimension corresponds to the largest ionic radii. The results explain that Li-ferrite has lowest fractal dimension and highest porosity, and a bigger crystal size of around 35 nm. Cu-ferrite showed the lowest crystallite size of around 13 nm with higher residual strain, while Cd-ferrite has the highest residual strain. It can be concluded that the small residual strain is related to the lowest surface energy since the particles tend to locate themselves in the position that decreases the surface energy to maximize stabilization. It is also noted that the porosity of the ferrites decreases with increasing the fractal dimension.

**Acknowledgments** The authors are very thankful for Dr. Emad El-Menyawy, Solid State Department, National Research Center, Giza , Egypt for fruitful discussion.

## References


1. Abdellatif M, Abdelrasoul GN, Scarpellini A, Marras S, Diaspro A (2015) Induced growth of dendrite gold nanostructure by controlling self-assembly aggregation dynamics. J Colloid Interface Sci, 458. https://doi.org/10.1016/j.jcis.2015.07.055
2. Abdellatif M, Song JD, Choi WJ, Cho NK, Lee JI (2010) Evidence of correlated electron hole pairs in dots in asymmetric quantum well structures. J Phys Conf Ser, 244. https://doi.org/10.1088/1742-6596/245/1/012050
3. Abdellatif M, Abdelrasoul GN, Salerno M, Liakos I, Scarpellini A, Marras S, Diaspro A (2016) Fractal analysis of inter-particle interaction forces in gold nanoparticle aggregates, Colloids Surfaces A Physicochem. Eng Asp 497:225–232. https://doi.org/10.1016/j.colsurfa.2016.03.013
4. Sederberg S, Elezzabi AY (2011) Sierpiński fractal plasmonic antenna: a fractal abstraction of the plasmonic bowtie antenna. Opt Express 19:10456. https://doi.org/10.1364/OE.19.010456
5. Abdellatif M, Salerno M, Abdelrasoul GN, Liakos I, Scarpellini A, Marras S, Diaspro A (2016) Effect of Anderson localization on light emission from gold nanoparticle aggregates, Beilstein. J Nanotechnol 7:2013–2022. https://doi.org/10.3762/bjnano.7.192
6. abdellatif MH Fractal Phenomena In The Nanoparticles Aggregation / 978-3-330-04153-0/9783330041530/3330041536,LaPLambert Academic Publishing, 2017. https://www.lap-publishing.com/catalog/details//store/tr/book/978-3-330-04153-0/fractal-phenomena-in-the-nanoparticles-aggregation (accessed March 2, 2017)
7. Mandelbrot BB (1983) The fractal geometry of nature. Am J Phys 51:286. https://doi.org/10.1119/1.13295
8. Meiwes-Broer K-H (2000) Metal clusters at surfaces. Springer Berlin Heidelberg, Berlin Heidelberg. https://doi.org/10.1007/978-3-642-57169-5
9. Bréchignac C., Houdy P., Lahmani M. (eds) (2007) Nanomaterials and nanochemistry. Springer Berlin Heidelberg, Berlin Heidelberg. https://doi.org/10.1007/978-3-540-72993-8
10. Family F (1996) Fractal concepts in surface growth. J Stat Phys 83:1255–1259. https://doi.org/10.1007/BF02179563
11. Wu KH, Ting TH, Li MC, Ho WD (2006) Sol–gel auto-combustion synthesis of SiO2-doped NiZn ferrite by using various fuels. J Magn Magn Mater 298:25–32. https://doi.org/10.1016/j.jmmm.2005.03.008
12. Kumar ER, Kamzin AS, Prakashc T (2015) Effect of particle size on structural, magnetic and dielectric properties of manganese substituted nickel ferrite nanoparticles. J Magn Magn Mater 378:389–396. https://doi.org/10.1016/J.JMMM.2014.11.019
13. Sutka A, Mezinskis G (2012) Sol-gel auto-combustion synthesis of spinel-type ferrite nanomaterials. Front Mater Sci 6:128–141. https://doi.org/10.1007/s11706-012-0167-3
14. Hwang C-C, Tsai J-S, Huang T-H (2005) Combustion synthesis of Ni–Zn ferrite by using glycine and metal nitrates—investigations of precursor homogeneity, product reproducibility, and reaction mechanism. Mater Chem Phys 93:330–336. https://doi.org/10.1016/j.matchemphys.2005.03.056
15. Ahmed TT, Rahman IZ, Rahman MA (2004) Study on the properties of the copper substituted NiZn ferrites. J Mater Process Technol 153–154:797–803. https://doi.org/10.1016/j.jmatprotec.2004.04.188
16. Mouallem-Bahout M, Bertrand S, Peña O (2005) Synthesis and characterization of Zn1-xNixFe2O4 spinels prepared by a citrate precursor. J Solid State Chem 178:1080–1086. https://doi.org/10.1016/j.jssc.2005.01.009
17. Ahmed MA, Afify HH, El Zawawia IK, Azab AA (2012) Novel structural and magnetic properties of Mg doped copper nanoferrites prepared by conventional and wet methods. J Magn Magn Mater 324:2199–2204. https://doi.org/10.1016/j.jmmm.2012.02.025
18. Aruna ST, Mukasyan AS (2008) Combustion synthesis and nanomaterials. Curr Opin Solid State Mater Sci 12:44–50. https://doi.org/10.1016/j.cossms.2008.12.002
19. Randhawa BS, Dosanjh HS, Kumar N (2007) Synthesis of lithium ferrite by precursor and combustion methods: A comparative study. J Radioanal Nucl Chem 274:581–591. https://doi.org/10.1007/s10967-006-6924-y
20. Sutka A, Gross KA, Mezinskis G, Bebris G, Knite M (2011) The effect of heating conditions on the properties of nano- and microstructured Ni–Zn ferrite. Phys Scr 83:25601. https://doi.org/10.1088/0031-8949/83/02/025601
21. Nayak PK (2008) Synthesis and characterization of cadmium ferrite. Mater Chem Phys 112:24–26. https://doi.org/10.1016/j.matchemphys.2008.05.018
22. Shobana MK, Rajendran V, Jeyasubramanian K, Suresh Kumar N (2007) Preparation and characterisation of NiCo ferrite nanoparticles. Mater Lett 61:2616–2619. https://doi.org/10.1016/j.matlet.2006.10.008
23. Mallapur MM, Shaikh PA, Kambale RC, Jamadar HV, Mahamuni PU, Chougule BK (2009) Structural and electrical properties of nanocrystalline cobalt substituted nickel zinc ferrite. J Alloys Compd 479:797–802. https://doi.org/10.1016/j.jallcom.2009.01.142
24. Yue Z, Guo W, Zhou J, Gui Z, Li L (2004) Synthesis of nanocrystilline ferrites by sol–gel combustion process: the influence of pH value of solution. J Magn Magn Mater 270:216–223. https://doi.org/10.1016/j.jmmm.2003.08.025
25. Azadmanjiri J, Salehani HK, Barati MR, Farzan F (2007) Preparation and electromagnetic properties of Ni1-xCuxFe2O4 nanoparticle ferrites by sol–gel auto-combustion method. Mater Lett 61:84–87. https://doi.org/10.1016/j.matlet.2006.04.011
26. Witten T, Sander L (1981) Diffusion-limited aggregation, a kinetic critical phenomenon. Phys Rev Lett 47:1400–1403. https://doi.org/10.1103/PhysRevLett.47.1400
27. Fernández-Martínez M, Sánchez-Granero MA (2014) Fractal dimension for fractal structures. Topol Appl 163:93–111. https://doi.org/10.1016/j.topol.2013.10.010
28. Mandelbrot BB (2006) Self-affine fractals and fractal dimension. Phys Scr 32:257–260. https://doi.org/10.1088/0031-8949/32/4/001
29. Grassberger P (1981) On the Hausdorff dimension of fractal attractors. J Stat Phys 26:173–179. https://doi.org/10.1007/BF01106792
30. Viswanathan B, Murthy VRK (1990) Ferrite materials?: science and technology, Narosa Pub House
31. Snelling EC (1969) Soft ferrites: properties and applications, Iliffe
32. Abdellatif Mohamed MA Ferrites, Theory and Applications, 978-3-330-07427-9, 3330074272 ,9783330074279 by Mohamed Abdellatif, Aisha Moustafa, LAP LAMPERT Academic publishing, 2017. https://www.morebooks.de/store/gb/book/ferrites,-theory-and-applications/isbn/978-3-330-07427-9 (accessed May 26, 2017)
33. Kumar ER, Reddy PSP, Devi GS (2016) Structural and Gas Sensing Properties of Mn Substituted

ZnFe<SUB>2</SUB>O<SUB>4</SUB> Nanoparticles by Auto Combustion and Evaporation Method. J Adv Phys 5:230–235. https://doi.org/10.1166/jap.2016.1259
34. Sekhon JS, Verma S (2011) Optimal Dimensions of Gold Nanorod for Plasmonic Nanosensors. Plasmonics 6:163–169. https://doi.org/10.1007/s11468-010-9182-3
35. Shannon RD (1976) IUCr, Revised effective ionic radii and systematic studies of interatomic distances in halides and chalcogenides. Acta Crystallogr Sect A 32:751–767. https://doi.org/10.1107/S0567739476001551
36. Family F, Vicsek T (1985) Scaling of the active zone in the Eden process on percolation networks and the ballistic deposition model. J Phys A Math Gen 18:L75–L81. https://doi.org/10.1088/0305-4470/18/2/005
37. Kamzin AS, Ranjith Kumar E, Ramadevi P, Selvakumar C (2017) The properties of Mn–CuFe2O4 spinel ferrite nanoparticles under various synthesis conditions. Phys Solid State 59:1841–1851. https://doi.org/10.1134/S1063783417090128
38. Verma S, Karande J, Patidar A, Joy PA (2005) Low-temperature synthesis of nanocrystalline powders of lithium ferrite by an autocombustion method using citric acid and glycine. Mater Lett 59:2630–2633. https://doi.org/10.1016/j.matlet.2005.04.005
39. Salunkhe AB, Khot VM, Phadatare MR, Pawar SH (2012) Combustion synthesis of cobalt ferrite nanoparticles—Influence of fuel to oxidizer ratio. J Alloys Compd 514:91–96. https://doi.org/10.1016/j.jallcom.2011.10.094
40. Kumar ER, Reddy PSP, Devic GS, Sathiyaraj S (2016) Structural, dielectric and gas sensing behavior of Mn substituted spinel MFe2O4 (M=Zn, Cu, Ni, and Co) ferrite nanoparticles. J Magn Magn Mater 398:281–288. https://doi.org/10.1016/J.JMMM.2015.09.018
41. Abdellatif M, El-Komy GM, Azab AA, Moustafa AM (2017) Oscillator strength and dispersive energy of dipoles in ferrite thin film. Mater Res Express 4:76410. https://doi.org/10.1088/2053-1591/aa7e57
42. Abdellatif M, Azab AA, Salerno M (2018) Effect of rare earth doping on the vibrational spectra of spinel Mn-Cr ferrite. Mater Res Bull 97:260–264. https://doi.org/10.1016/j.materresbull.2017.09.012
43. Abdellatif MH, El-Komy GM, Azab AA, Salerno M (2018) Crystal field distortion of La3+ ion-doped Mn-Cr ferrite. J Magn Magn Mater 447:15–20. https://doi.org/10.1016/J.JMMM.2017.09.040
44. Abdellatif M, Azab AA, Moustafa AM (2017) Dielectric spectroscopy of localized electrical charges in ferrite thin film. J Electron Mater, pp 1–7. https://doi.org/10.1007/s11664-017-5782-4
45. Intartaglia R, Rodio M, Abdellatif M, Prato M, Salerno M (2016) Extensive characterization of oxide-coated colloidal gold nanoparticles synthesized by laser ablation in liquid. Mater 9:775.9. 775 https://doi.org/10.3390/MA9090775
46. Abdellatif M, Song JD, Choi WJ, Cho NK (2012) In/Ga interdiffusion in InAs quantum dot in InGaAs/GaAs asymmetric quantum well. J Nanosci Nanotechnol 12:5774–7